

Optical third-harmonic generation of fused silica in gas atmosphere: Absolute value of the third-order nonlinear optical susceptibility $\chi^{(3)}$

Ulrich Gubler* and Christian Bosshard

Nonlinear Optics Laboratory, Institute of Quantum Electronics, ETH Hönggerberg, CH-8093 Zürich, Switzerland

(Received 5 October 1999)

We report on a calibration procedure based on third-harmonic generation, which yields absolute values for $\chi^{(3)}$. By calibrating the nonlinear susceptibility $\chi^{(3)}$ of fused silica against the established, quantum chemically calculated second-order hyperpolarizabilities γ of various gases at different pressures, we determine reliable absolute values for fused silica. We propose a standard third-order nonlinear optical susceptibilities $\chi^{(3)}$ of fused silica $\chi^{(3)}(-3\omega, \omega, \omega, \omega) = (2.0 \pm 0.2) \times 10^{-22} \text{ m}^2/\text{V}^2$ at the wavelength $1.064 \mu\text{m}$ and $\chi^{(3)}(-3\omega, \omega, \omega, \omega) = (1.6 \pm 0.2) \times 10^{-22} \text{ m}^2/\text{V}^2$ at $1.907 \mu\text{m}$. These results are in excellent agreement with the cascading experiments reported by Bosshard *et al.* [Phys. Rev. B **61**, 10 688 (2000)].

I. INTRODUCTION

En route to all-optical signal processing, the development of materials with large third-order nonlinear optical effects is of decisive importance. For the material characterization and the assessment of its usefulness for applications, the absolute value of the third-order nonlinear optical susceptibility $\chi^{(3)}$ has to be known. Since most measurements are performed relative to a reference material, the establishment of a well-accepted value for a standard material is important.

The most widely employed material characterization techniques are third-harmonic generation (THG),¹ degenerate four-wave mixing (DFWM),² and the Z scan.³ In THG the frequency of the incoming beam is tripled by the nonlinear optical susceptibility $\chi^{(3)}(-3\omega, \omega, \omega, \omega)$. Only the instantaneous electronic effect can contribute to the nonlinearity. In DFWM and the Z scan, vibrational, orientational, and thermal effects can also contribute to the nonlinearity $\chi^{(3)}(-\omega, \omega, -\omega, \omega)$. By employing short laser pulses the latter two can be avoided. Because one needs fast nonlinearities for all-optical signal processing, our main interest is directed toward the fast electronic nonlinearities. Therefore, and also due to its simplicity, third-harmonic generation is a very attractive method to characterize newly developed materials.

For DFWM and the Z scan, standard values have been established. The liquid CS_2 is most commonly used as a reference material.³ As the nonlinear refractive index n_2 is proportional to the real part of the degenerate nonlinearity $\chi^{(3)}(-\omega, \omega, -\omega, \omega)$, it can also be used as a standard for $\chi^{(3)}(-\omega, \omega, -\omega, \omega)$:

$$n(I) = n_0 + n_2 I \quad (1)$$

$$n_2(\omega) = \frac{3}{4\varepsilon_0 c n_0^2} \text{Re}[\chi^{(3)}(-\omega, \omega, -\omega, \omega)]. \quad (2)$$

n_0 is the linear refractive index, I the intensity, ε_0 the dielectric constant in vacuum, and c the speed of light in vacuum. The nonlinear refractive index n_2 of fused silica has been measured by different methods, and a standard value has recently been reported.⁴

In third-harmonic generation experiments the situation is somewhat different. To date most people have used the value $\chi^{(3)}(-3\omega, \omega, \omega, \omega) = 3.89 \times 10^{-22} \text{ m}^2/\text{V}^2 = 2.79 \times 10^{-14} \text{ esu}$ of fused silica, which was obtained by cascading of second-order susceptibilities $\chi^{(2)}$.^{5,6} The values of the second-order susceptibilities $\chi^{(2)}$, on which this calibration approach is based, changed in past years, and more recent cascading experiments revealed a value of the third-order susceptibility $\chi^{(3)}(-3\omega, \omega, \omega, \omega)$ that is a factor 2.4–3 smaller than the original one.^{7,8}

Our idea here is to determine absolute third-order susceptibilities $\chi^{(3)}(-3\omega, \omega, \omega, \omega)$ in a direct approach, without the indirect path using the second-order susceptibilities $\chi^{(2)}$ in cascading experiments (Fig. 1). The second-order hyperpolarizability γ ($\chi^{(3)}$ per molecule instead of volume) of gas atoms or diatomic molecules has been calculated quantum mechanically,⁹ with a sufficient precision to make a calibra-

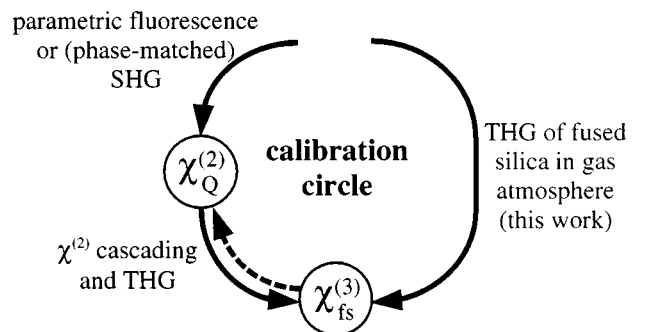


FIG. 1. Calibration scheme of optical third-order susceptibilities $\chi^{(3)}$ of fused silica. Pursuing the left path, the second-order susceptibility $\chi^{(2)}$ of a noncentrosymmetric material (quartz) has to be measured first by parametric fluorescence or (phase-matched) second-harmonic generation (SHG). Afterwards $\chi^{(3)}$ of this noncentrosymmetric material can be calibrated by cascading and finally a comparing third-harmonic generation (THG) measurement yields $\chi^{(3)}$ of fused silica. In this work we are following the right path, which allows us to determine $\chi^{(3)}$ of fused silica directly by comparing it with the nonlinearities of gases in a third-harmonic generation experiment. In the end we can also use the value of $\chi^{(3)}$ determined here to confirm the second-order susceptibility $\chi^{(2)}$ of quartz (dashed arrow).

tion within an error range of some percent feasible. With a third-harmonic generation measurement of a fused silica plate in a well-defined gas atmosphere, the ratio of the third-order susceptibility $\chi^{(3)}(-3\omega, \omega, \omega, \omega)$ of fused silica against the second-order hyperpolarizability $\gamma(-3\omega, \omega, \omega, \omega)$ of the involved gas atoms or molecules can be retrieved, and an absolute value for the nonlinearity $\chi^{(3)}$ determined.

With these independent measurements, we can assess the standard values and compare them with the values obtained earlier by cascading. This enables us to introduce a more reliable standard value of the third-order susceptibility $\chi^{(3)}(-3\omega, \omega, \omega, \omega)$ of fused silica. Furthermore, we can also confirm the second-order susceptibility $\chi^{(2)}$ of quartz, by taking our third-order susceptibility standard value $\chi^{(3)}$ from third-harmonic generation, and using the cascading experiments in the backward direction (Fig. 1) to calibrate $\chi^{(2)}$ against $\chi^{(3)}$.

II. THEORY

A. Definition of nonlinear optical coefficients

In nonlinear optics various conventions for the expansion of the polarization $\mathbf{P}(\mathbf{r}, t)$ and the electric fields $\mathbf{E}(\mathbf{r}, t)$ have been used. Nonlinearity values of different authors have to be compared carefully, paying attention to different definitions.

We define the electric fields $\mathbf{E}(\mathbf{r}, t)$ and polarization $\mathbf{P}(\mathbf{r}, t)$ propagating in the z direction in an isotropic medium as

$$\mathbf{E}(\mathbf{r}, t) = \frac{1}{2} \sum_m \{ \mathbf{E}_m(\mathbf{r}, \omega_m) \exp[i(k_m z - \omega_m t)] + \text{c.c.} \}, \quad (3)$$

$$\mathbf{P}(\mathbf{r}, t) = \frac{1}{2} \sum_{m'} \{ \mathbf{P}_{m'}(\mathbf{r}, \omega_{m'}) \exp[i(k_{m'} z - \omega_{m'} t)] + \text{c.c.} \}, \quad (4)$$

where c.c. denotes the complex conjugate of the first term, $k_m = (\omega/c)n_m$ the wave vector, and $\mathbf{E}_m(\mathbf{r}, \omega_m)$ the complex electric field amplitudes. For the expansion of the polarization amplitudes (assuming summation over common indices), we write

$$P_i = P_{0,i} + \varepsilon_0 \{ \chi_{ij}^{(1)} E_j + \chi_{ijk}^{(2)} E_j E_k + \chi_{ijkl}^{(3)} E_j E_k E_l + \dots \}, \quad (5)$$

with \mathbf{P}_0 the spontaneous polarization and $\chi^{(n)}$ the n th-order susceptibility. For the atomic or molecular hyperpolarizabilities, the analogous definition is

$$p_i = \mu_i + \varepsilon_0 \{ \alpha_{ij} E_j + \beta_{ijk} E_j E_k + \gamma_{ijkl} E_j E_k E_l + \dots \}, \quad (6)$$

with \mathbf{p} the microscopic molecular polarization, μ the molecular dipole moment, α_{ij} the polarizability, β_{ijk} the first-order hyperpolarizability, and γ_{ijkl} the second-order hyperpolarizability. In quantum-chemical calculations of the hyperpolarizabilities $\tilde{\beta}$ and $\tilde{\gamma}$, different definitions of the polarization expansion are used:⁹

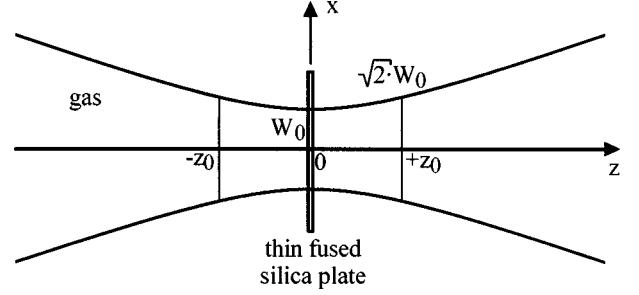


FIG. 2. Geometry of the third-harmonic generation experiments. A thin fused silica plate is placed in the focus of a Gaussian beam with the beam waist W_0 . The focal parameter z_0 is significantly larger than the plate thickness L . Surrounding the fused silica plate is a gas atmosphere with well-defined parameters.

$$p_i = \mu_i + \varepsilon_0 \left(\alpha_{ij} E_j + \frac{\tilde{\beta}_{ijk}}{2!} E_j E_k + \frac{\tilde{\gamma}_{ijkl}}{3!} E_j E_k E_l + \dots \right), \quad (7)$$

$$\gamma_{ijkl} = \tilde{\gamma}_{ijkl}/6. \quad (8)$$

The factor 6 has to be considered when comparing absolute values of the third-order nonlinear optical properties with the two different definitions.

Summing over all possible terms, the relevant polarization of third-harmonic generation consequently results in

$$P_i^{3\omega} = \frac{\varepsilon_0}{4} \chi_{iiii}^{(3)}(-3\omega, \omega, \omega, \omega) E_i^\omega E_i^\omega E_i^\omega = \frac{\varepsilon_0}{4} \chi^{(3)} E_\omega^3. \quad (9)$$

The indices in Eq. (9) are omitted on the right side of the equation to simplify the notation. In the following equations the term $\chi^{(3)}$ will always refer to the use in Eq. (9), if not explicitly defined otherwise. Since we have a nearly ideal gas (see Sec. III D), the relation between the macroscopic third-order susceptibility $\chi^{(3)}$ and the microscopic molecular second-order hyperpolarizability γ is given by

$$\chi^{(3)}(-3\omega, \omega, \omega, \omega) = N f_{\omega,3\omega}^3 \gamma(-3\omega, \omega, \omega, \omega), \quad (10)$$

$$f_{\omega,3\omega} = \frac{n_{\omega,3\omega}^2 + 2}{3}, \quad (11)$$

where N is the number of molecules per volume, and $f_{\omega,3\omega}$ are the local-field factors in the Lorentz approximation. With the molecular density N and the refractive indices $n_{\omega,3\omega}$ depending on the pressure p in the gas phase, the third-order susceptibility $\chi^{(3)}$ is a function of p as shown below. Since $n_{\omega,3\omega}$ of the gas atmospheres in our experiments are almost 1, the local-field factors are close to unity, and can be omitted in practice.

B. Third-harmonic generation by a Gaussian beam

In the third-harmonic generation experiment a Gaussian laser beam is focused on a fused silica plate placed in the focus (Fig. 2). The electric-field amplitude E_ω of the incident Gaussian beam with the beam waist at $z=0$ is

$$E_\omega(r) = \frac{E_0}{1 + iz/z_0} \exp\left(-\frac{k_\omega \rho^2}{2z_0(1 + iz/z_0)}\right), \quad (12)$$

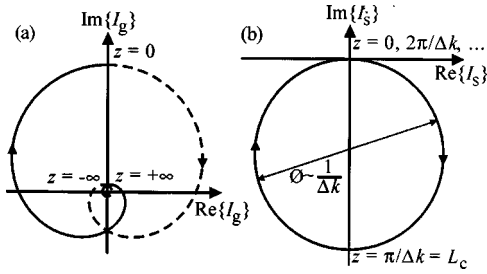


FIG. 3. Traces of the third-harmonic-generation integral $I_{s,g}(z)$, according to Eqs. (15) and (16), for a negative wave-vector difference of fundamental and harmonic frequencies $\Delta k = k_{3\omega} - 3k_\omega < 0$. (a) For an infinite medium the integration up to the focus yields a pure imaginary value. The integration over the whole space leads back to zero, with no net third harmonic generated. (b) For a thin plate in the focus, the integral is a periodic function describing a circle in the complex plane. Its diameter \varnothing is inversely proportional to Δk .

where $\rho = \sqrt{x^2 + y^2}$ is the radial coordinate, $z_0 = \pi W_0^2 / \lambda$ the focal parameter, W_0 the beam waist in the focus, $k_\omega = (\omega/c)n_\omega$ the wave vector of the initial beam, and E_0 the maximal electric-field amplitude in the beam waist. The created third-harmonic beam $E_{3\omega}$ between a lower boundary $z = a$ and z results in¹⁰⁻¹²

$$E_{3\omega}(\mathbf{r}) = i \frac{C(\mathbf{r})}{n_{3\omega}} \chi^{(3)} E_0^3 \int_a^z \frac{e^{i\Delta k(z'-a)}}{(1+iz'/z_0)^2} dz', \quad (13)$$

$$C(\mathbf{r}) = \frac{3}{8} \frac{\omega}{c} \frac{1}{1+iz/z_0} \exp\left(-\frac{3k_\omega \rho^2}{2z_0(1+iz/z_0)}\right), \quad (14)$$

where $\Delta k = 3k_\omega - k_{3\omega} = 3\omega/c(n_\omega - n_{3\omega})$ is the wave-vector difference. The term $C(\mathbf{r})$ is easily calculated and will not be discussed any further. The integral

$$I_g(z) = \int_a^z \frac{e^{i\Delta k(z'-a)}}{(1+iz'/z_0)^2} dz' \quad (15)$$

can only be solved numerically for general integration boundaries, and is usually visualized in vibration diagrams¹⁰ (see the Appendix). The integral $I_g(z)$ is plotted in the complex plane as a function of z , with the resulting harmonic amplitude being the vector from the origin to the end point of the trace. An integration over the infinite medium yields the vibration diagram depicted in Fig. 3, with no net third-harmonic generation. The integration over the negative half-space $z < 0$ yields a spiral with the end point on the imaginary axis. If the integral is continued to $+\infty$, another, horizontally flipped, spiral turns back to zero. As $I_g(z=0)$ is purely imaginary and positive for $\Delta k_g < 0$, the sign of $E_{3\omega}$ at $z=0$ is negative [Eq. (13)], compared to the positive sign of E_ω . This corresponds to a phase shift of π between fundamental and harmonic field. Because of symmetry, the positive half-space $0 < z < \infty$ then has to cancel the created third harmonic of the negative half-space.

The situation changes if a thin plate with thickness L is placed in the focus. The integration in the gas phase is still conducted up to zero instead of $-L/2$, which introduces a negligible error (see the Appendix). If the thickness L of the

plate is much less than the focal parameter z_0 ($L \ll z_0$), the integrand can be simplified and the integral $I_s(L)$ solved analytically,

$$\begin{aligned} I_s(L) &= \int_{-L/2}^{L/2} \frac{e^{i\Delta k_s(z'+L/2)}}{(1+iz'/z_0)^2} dz' \approx e^{i\Delta k_s L/2} \int_{-L/2}^{L/2} e^{i\Delta k_s z'} dz' \\ &= e^{i\Delta k_s L/2} \frac{2 \sin(\Delta k_s L/2)}{\Delta k_s}, \end{aligned} \quad (16)$$

yielding the same result as third-harmonic generation for plane waves.¹ The approximation in Eq. (16) is discussed in more detail in the Appendix. The integral $I_s(L)$ describes a circle in the lower complex plane [Fig. 3(b)], with the periodicity $2\pi/\Delta k_s$ in the plate thickness L . The length $L_c = \pi/\Delta k_s$ for the generation of the maximal third-harmonic signal is usually called the coherence length.

After the plate, the spiral of the gas in the positive half-space $0 < z < \infty$ turns back to the inside of the circle of fused silica (Fig. 4). Because the phase shift between the fundamental and harmonic electric field at the endface of the plate is no longer π , the spiral is not just horizontally flipped, but also rotated by this phase difference compared to the spiral of the negative half-space. Including the transmission factors $t^{\omega,3\omega}$ for the fundamental and harmonic frequencies,

$$t_{gs}^{\omega,3\omega} = \frac{2n_g^{\omega,3\omega} \cos \theta_g}{n_g^{\omega,3\omega} \cos \theta_g + n_s^{\omega,3\omega} \cos \theta_s^{\omega,3\omega}}, \quad (17)$$

$$t_{sg}^{\omega,3\omega} = \frac{2n_s^{\omega,3\omega} \cos \theta_s^{\omega,3\omega}}{n_g^{\omega,3\omega} \cos \theta_g + n_s^{\omega,3\omega} \cos \theta_s^{\omega,3\omega}}, \quad (18)$$

$$n_g^{\omega,3\omega} \sin \theta_g = n_s^{\omega,3\omega} \sin \theta_s^{\omega,3\omega} \quad (\text{Snellius}), \quad (19)$$

with the external (internal) angle of incident $\theta_g(\theta_s)$, the trace of the generated third-harmonic $E_{3\omega}$ in the complex plane follows, as sketched in Fig. 4:

$$\begin{aligned} E_{3\omega}(\mathbf{r}) &= iC(\mathbf{r})E_0^3 \left(\frac{\chi_g^{(3)}}{n_g^{3\omega}} I_g(0) [t_{gs}^{3\omega} t_{sg}^{\omega,3\omega} \right. \\ &\quad \left. + (t_{gs}^{\omega,3\omega})^3 (t_{sg}^{\omega,3\omega})^3 e^{i(\Delta k_s L - \pi/2)}] \right. \\ &\quad \left. + \frac{\chi_s^{(3)}}{n_s^{3\omega}} (t_{gs}^{\omega,3\omega})^3 t_{sg}^{\omega,3\omega} \frac{2 \sin(\Delta k L/2)}{\Delta k} e^{i\Delta k L/2} \right). \end{aligned} \quad (20)$$

In Eq. (20) we have two terms which contribute to the third-harmonic signal $E_{3\omega}$: one from the gas and one from the solid. By rotating the plate the interaction length in the solid is changed, and the signal $E_{3\omega}$ pursues the dotted circle in Fig. 4, showing the well known Maker-fringe pattern in the experiment. By measuring the plate in vacuum, and afterwards at different gas pressures, the two contribution can be separated and calibrated against one another.

III. EXPERIMENTAL METHOD

A. Third-harmonic generation setup

For the third-harmonic generation measurements, a pulsed Nd:YAG (yttrium aluminum garnet) laser with a pulse width of 5 ns is employed (Fig. 5). Either the fundamental wave-

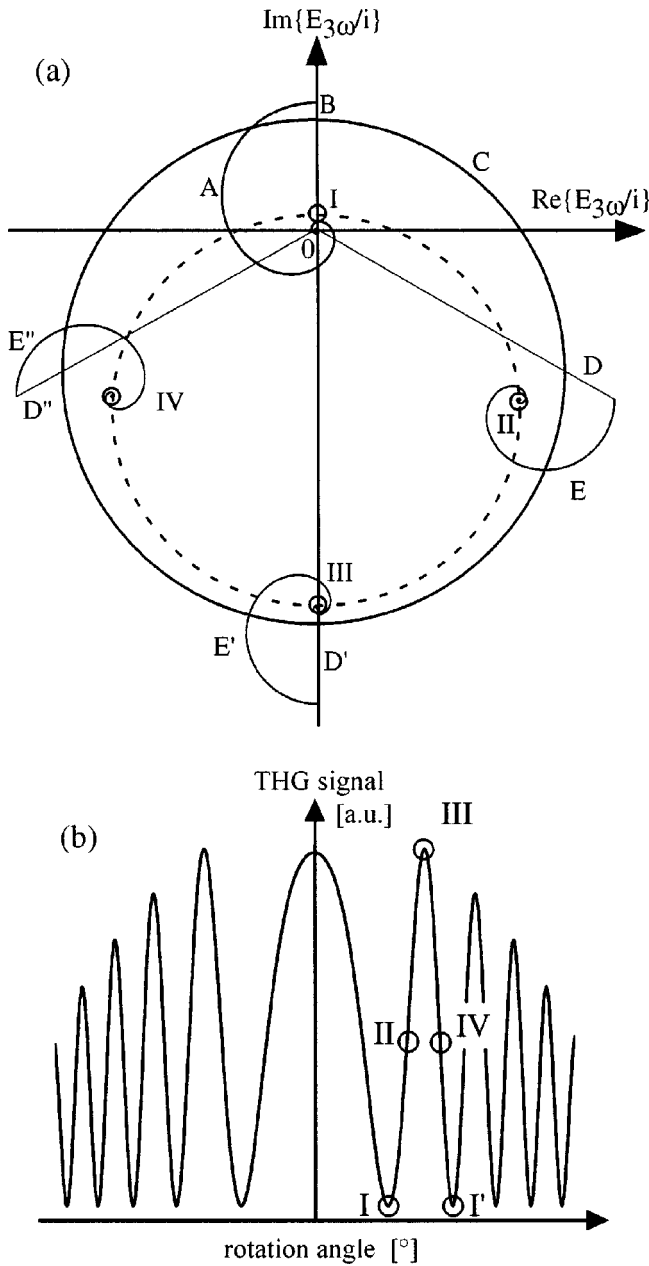


FIG. 4. Generated third-harmonic field $E_{3\omega}$ in the complex plane for the experimental geometry in Fig. 2. (a) The gas in the negative half-space ($z < 0$) creates a third-harmonic signal (A), which is reduced by the transmission factor at the fused silica interface (B). In the fused silica the generated third harmonic describes a circle in the complex plane as a function of its thickness (C). After transmission out of the fused silica (D, D', and D''), the gas in the positive half-space ($z > 0$) adds an additional contribution to the generated third-harmonic frequency (E, E', and E''). By changing the thickness of the fused silica plate, the signal $E_{3\omega}$ follows the dashed circle. (b) If the optical path length through the thin fused silica plate is changed by rotation, the third-harmonic-generation signal ($\sim |E_{3\omega}|^2$) oscillates as a function of the angle as depicted in Fig. 4(a), according to the Maker-fringe patterns. The decrease of the THG signal in the wings originates in the smaller transmission factors for increasing angles, which is not depicted in (a).

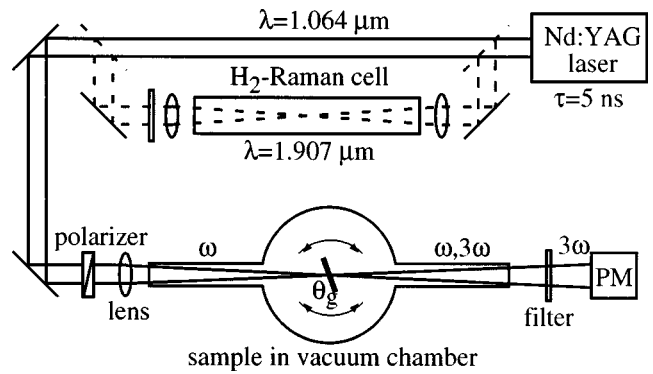


FIG. 5. In the THG setup a Nd:YAG laser ($\lambda = 1.064 \mu\text{m}$) with 5-ns pulses is either injected directly in the experiment or frequency shifted by a H_2 Raman cell to the wavelength $\lambda = 1.907 \mu\text{m}$. The beam is polarized parallel to the rotation axis of the fused silica plate (*s* polarized), and focused in the gas chamber. The thin fused silica plate is mounted on a rotation stage in the focus of the laser beam. After the THG, the fundamental beam is removed with filters and the THG signal measured with a photomultiplier (PM).

length $\lambda = 1.064 \mu\text{m}$ or the H_2 -Raman shifted wavelength $\lambda = 1907 \mu\text{m}$ is used. The beam is polarized parallel to the rotation axis of the fused silica plate (*s* polarized). The beam is focused with a 500-mm lens on a 1-mm-thick fused silica plate, which is placed on a rotation stage in a vacuum chamber. The windows are 450 mm apart, creating no detectable third-harmonic signal. The focal parameter z_0 is around 10–15 mm, which is well above the plate thickness and well below the chamber dimensions. After the chamber, the fundamental frequency is removed with filters, and the harmonic frequency detected with a photomultiplier. The photomultiplier signal is measured by a boxcar integrator, and acquired on a computer, which also drives the rotation stage. To account for the laser power fluctuations, the third-harmonic

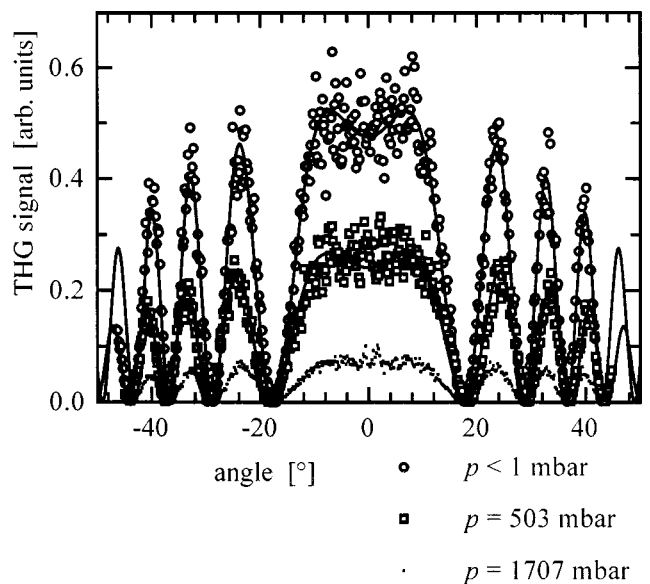


FIG. 6. Measurement curves of the THG experiments. The amplitude of the Maker-fringe curves is decreased with increasing gas pressure, as this example with nitrogen shows. The data analysis of a pressure series yields the ratio of the gas and fused silica nonlinearities (Fig. 10).

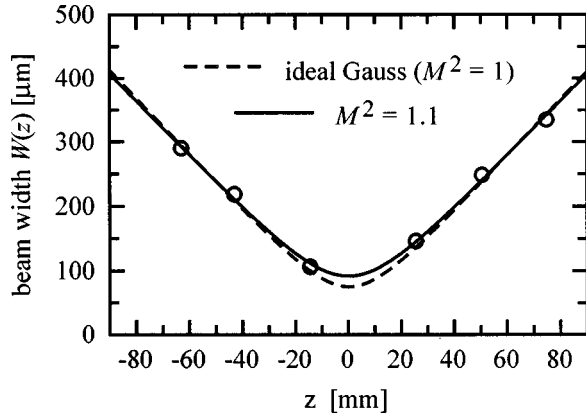


FIG. 7. The laser beam deviates slightly from an ideal Gaussian beam. The analysis of the beam waist vs propagation distance z with Eq. (22) yields $M^2=1.1$ at the wavelength $\lambda=1.064\ \mu\text{m}$. The beam quality is difficult to improve further, and is the main error source in the calibration experiments.

signal is measured relative to the one generated in a second sample and divided pulse by pulse. This second THG line is not depicted in Fig. 5.

By rotating the plate, Maker-fringe patterns are obtained (Fig. 6) and analyzed according to Eq. (20). In the experimental procedure, a fused silica measurement in vacuum ($p < 1$ mbar) is taken first. Afterwards, measurements in various gas atmospheres are performed, up to a pressure $p = 2000$ mbar. The pressure-dependent ratio

$$\frac{\chi_g^{(3)} I_g(0)}{\chi_s^{(3)}} \quad (21)$$

can be determined by using Eq. (20) and the fused silica measurements in vacuum.

To validate our experiment series, we performed measurements on different gas molecules. The rare gases helium and argon and the diatomic molecules hydrogen H_2 and nitrogen N_2 were studied. The results from the different gas species should yield the same calibration results for fused silica.

B. Gaussian beam profile

To evaluate the numerical integral $I_g(z=0)$, a Gaussian beam is assumed above, which is impossible to reach perfectly in reality. The Gaussian outcoupling mirror of our laser provides nearly Gaussian beams at the wavelength $\lambda = 1.064\ \mu\text{m}$. The beam was analyzed in the vacuum cham-

ber by cutting the beam with a razor blade perpendicular to the propagation direction at several positions around the focus. The pulse energies were measured as a function of the blade position with a pyroelectric Joulemeter. The beam width $W(z)$ was determined by applying the error function (integrated Gaussian function). Cuts close to the focus somewhat destroyed the edge of the razor blade. Also, at low powers close to the detection limit of the Joulemeter, metal ablation by the laser can be observed at the blade edge under a microscope. Therefore, the beam width we measured close to the focus may be too large, yielding a worse Gaussian beam in our analysis than it is in reality.

We assess our Gaussian beam quality, by applying the function

$$W(z) = M^2 W_0 \left[1 + \left(\frac{z}{z_0} \right)^2 \right]^{1/2}, \quad (22)$$

to the beam width vs propagation direction (Fig. 7). W_0 is the beam width in the focus, and M^2 is a parameter, describing the beam quality. An ideal Gaussian beam would correspond to $M^2=1$. For the wavelength $\lambda=1.064\ \mu\text{m}$ we find M^2 between 1.1 and 1.2.

The beam quality at the wavelength $\lambda=1.907\ \mu\text{m}$ is additionally decreased by the frequency shifting in the H_2 Raman cell. We find M^2 values between 1.2 and 1.3.

Simulations of the integral $I_g(z=0)$ for different focal parameters z_0 revealed only a slight dependence in z_0 . An error bar of 10% for the wavelength $\lambda=1.064\ \mu\text{m}$ and 15% for $\lambda=1.907\ \mu\text{m}$ have been shown to be sufficient to account for the imperfect beam quality. This error source is the main uncertainty in the measurement procedure and dominates the calibration error bar.

C. Hyperpolarizabilities of gas species

The nonlinear optical second-order hyperpolarizabilities γ of various atoms and small molecules have been calculated in the static limit of zero frequency.⁹ For the atoms and diatomic molecules we are investigating, the dispersions have also been determined. We calculated the nonlinearities at the experimental frequencies according to Ref. 9 (also see Table I). The hyperpolarizabilities γ add up independently to the third-order susceptibilities $\chi^{(3)}$ according to Eq. (10), where the molecular density $N(p)$ (see below) and the refractive indices $n_{\omega,3\omega}(p)$ are functions of the pressure in the chamber of the THG experiment.

TABLE I. Calculated atomic and molecular second-order hyperpolarizabilities γ in the static limit and at the experimental wavelengths (Ref. 9). The nonlinearities of the reference have to be changed from atomic units to SI units ($1\ \text{a.u.} = 7.0423 \times 10^{-54}\ \text{m}^5/\text{V}^2$) and divided by a factor of 6 due to the different conventions (Eqs. (6)–(8)).

Gas	$\tilde{\gamma}_{\text{static}}$ (a.u.)	γ_{static} (a.u.)	γ_{static} ($10^{-54}\ \text{m}^5/\text{V}^2$)	γ (1.907 μm) ($10^{-54}\ \text{m}^5/\text{V}^2$)	γ (1.064 μm) ($10^{-54}\ \text{m}^5/\text{V}^2$)
He	43.15	7.192	50.64	51.4	53.2
Ar	1220	203	1430	1480	1620
H_2	683	114	801	837	927
N_2	1010	168	1190	1220	1320

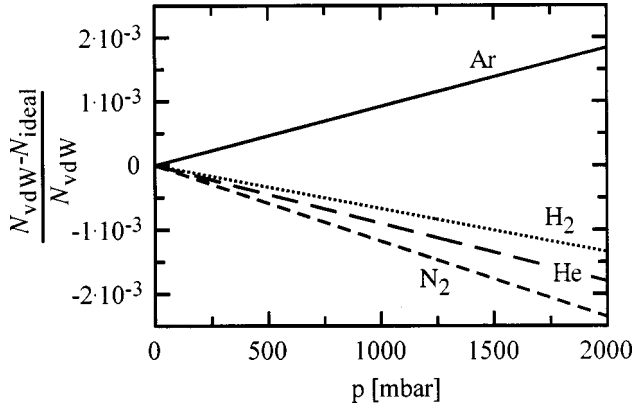


FIG. 8. Deviations of the calculated molecular densities N (number of molecules per volume) between the ideal gas model and the van der Waals gas as a function of the pressure p . The differences are in the range of per mills, and therefore much smaller than the experimental error.

D. Ideal vs van der Waals gas

For an ideal gas, the molecular density $N(p, T)$ can be expressed as

$$N(p, T) = p/k_B T, \quad (23)$$

with the Boltzmann constant k_B . Using the van der Waals equation as a more realistic gas model, the molecular density $N(p, T)$ can be retrieved by numerically solving

$$(p + N^2 a) \left(\frac{1}{N} - b \right) = k_B T, \quad (24)$$

with a and b two parameters tabulated for various gases in the literature.¹³ Comparison of the ideal and van der Waals models disclose only minor differences (below 0.25%) for the investigated pressures up to 2000 mbar (Fig. 8). To reduce computation time in the data analysis, we worked with the ideal gas equation and did not numerically solve the van der Waals equation.

E. Refractive indices

Refractive indices of the investigated gases have been measured in the visible and in the near infrared by different authors.^{14–18} The extrapolation to the longest wavelength $\lambda = 1.907 \mu\text{m}$ is believed to be accurate, as no infrared active vibration occurs for He, Ar, H_2 , and N_2 .

Since all refractive indices of the gases are very close to 1, they have no significant influence on the transmission coefficients $t^{\omega, 3\omega}$ [Eqs. (17) and (18)] and the local field cor-

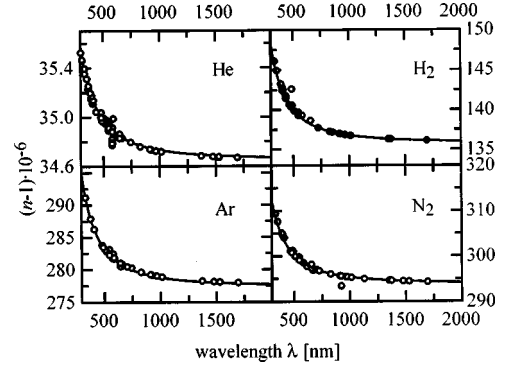


FIG. 9. Refractive index dispersion for the four investigated gas species. The measured data points from the literature are interpolated to the employed wavelengths in the THG experiments.

rections $f_{\omega, 3\omega}$ [Eq. (11)]. The only really dependent variable is the wave-vector difference $\Delta k = (3\omega/c)(n_\omega - n_{3\omega})$. Therefore, the dispersion of the nonlinear refractive index is of main interest and the absolute values of lower importance (see Fig. 9).

The refractive indices at standard conditions ($p_0 = 1 \text{ atm}$, $T_0 = 0^\circ \text{C}$) in Table II have to be transformed to the pressure and temperature in the experiment. As for the hyperpolarizabilities, the linear polarizabilities α add independently to the linear susceptibility $\chi^{(1)}$:

$$\chi^{(1)}(-\omega, \omega) = N f_\omega \alpha(-\omega, \omega) = n_\omega^2 - 1. \quad (25)$$

From the local-field corrections [Eq. (11)], and by referring to the standard conditions as mentioned above, it follows that

$$\frac{n^2 - 1}{n^2 + 2} = N \alpha / 3 = N \text{ const}, \quad (26)$$

$$\frac{n^2 - 1}{n^2 + 2} = \frac{N}{N_0} \frac{n_0^2 - 1}{n_0^2 + 2}, \quad (27)$$

$$n = \left[\left(1 + 2 \frac{N}{N_0} \frac{n_0^2 - 1}{n_0^2 + 2} \right) / \left(1 - \frac{N}{N_0} \frac{n_0^2 - 1}{n_0^2 + 2} \right) \right]^{1/2}. \quad (28)$$

For molecular densities N , either the equation for an ideal [Eq. (23)] or the van der Waals [Eq. (24)] gas can be deployed. For fused silica the refractive indices $n(354.7 \text{ nm}) = 1.476 24$, $n(635.7 \text{ nm}) = 1.456 99$, $n(1064 \text{ nm}) = 1.449 69$, and $n(1907 \text{ nm}) = 1.439 59$, from Sellmeier dispersion formulas, are used.¹⁴

TABLE II. Interpolated and extrapolated refractive indices n_0 at standard conditions ($p_0 = 1 \text{ atm}$, $T_0 = 0^\circ \text{C}$) (Refs. 14–18).

Gas	$(n_0 - 1) \times 10^{-6}$ $\lambda = 354.7 \text{ nm}$	$(n_0 - 1) \times 10^{-6}$ $\lambda = 635.7 \text{ nm}$	$(n_0 - 1) \times 10^{-6}$ $\lambda = 1064 \text{ nm}$	$(n_0 - 1) \times 10^{-6}$ $\lambda = 1907 \text{ nm}$
He	35.308	34.852	34.721	34.672
Ar	289.543	280.973	278.608	277.718
H_2	144.579	138.350	136.656	136.021
N_2	306.932	297.710	295.161	294.202

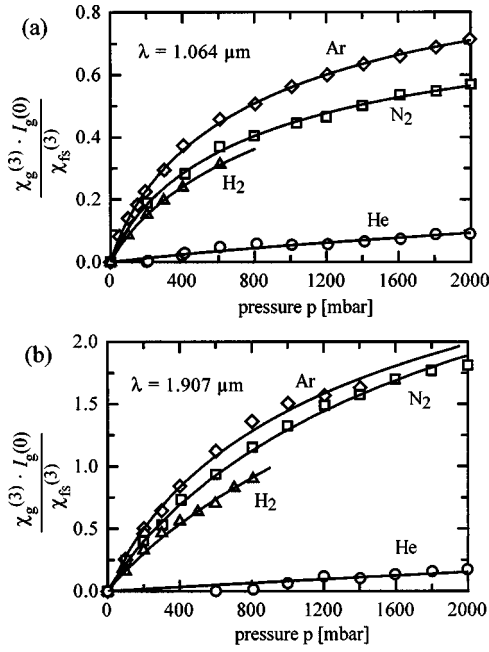


FIG. 10. Nonlinearity ratios [Eq. (21)] of the four investigated gas species vs the pressure in the THG chamber at wavelengths of $1.064 \mu\text{m}$ (a) and $1.907 \mu\text{m}$ (b). The evaluation of the measured ratios, indicated by the lines, yields the calibration values for the third-order susceptibility $\chi^{(3)}$ of fused silica.

IV. RESULTS AND DISCUSSION

The evaluations of the THG measurements yield the ratios [Eq. (21)] of the gas and fused silica contributions to the third harmonic signal (Fig. 10). The magnitude of the nonlinearity ratio originates in $\chi_g^{(3)}/\chi_{fs}^{(3)}$ and the curvature depends on the wave-vector difference Δk_g and the focal parameter z_0 . To determine the calibration values of the third-order susceptibility $\chi_{fs}^{(3)}$ the numerical integral I_g is fitted to the points in Fig. 10.

For argon, nitrogen, and hydrogen at the wavelength $\lambda = 1.064 \mu\text{m}$, it is possible to treat the focal parameter z_0 as a free parameter and determine it in the evaluation procedure of the nonlinearity ratio vs pressure. The resulting parameters z_0 are in agreement with the values determined from direct measurements with the razor blade. In the case of he-

lium, the standard deviation of a free running focal parameter z_0 increases dramatically, due to the very minor curvature in the data points. Therefore, the focal parameter is kept constant at the value determined by the measurements of the other three gases.

At a wavelength $\lambda = 1.907 \mu\text{m}$, the above analysis is no longer suitable. The diminished beam quality leads to larger standard deviations in the focal parameter z_0 . Consequently, we used the focal parameters from the Gaussian beam analysis of the beam cutting. The experimental error is enlarged as discussed above.

For both wavelengths the evaluated calibration values of fused silica determined with different gases are in good agreement with one another (Table III). All results are within the error bar of the average third-order susceptibility $\chi^{(3)}(-3\omega, \omega, \omega, \omega) = (2.04 \pm 0.20) \times 10^{-22} \text{ m}^2/\text{V}^2$ at $1.064 \mu\text{m}$, and $\chi^{(3)}(-3\omega, \omega, \omega, \omega) = (1.56 \pm 0.25) \times 10^{-22} \text{ m}^2/\text{V}^2$ at $1.907 \mu\text{m}$. The scattering at $\lambda = 1.907 \mu\text{m}$ is larger, as might be expected from the lower quality of the laser beam. The numbers for argon seem to be systematically larger than for the other gas species. One might speculate that its calculated hyperpolarizability γ is slightly too large. Furthermore, the calibration values determined with hydrogen at $\lambda = 1.907 \mu\text{m}$ are also somewhat lower than the average. Nevertheless, all these deviations are within the uncertainties expected from the nonideal Gaussian profile of our laser beam.

The comparison with our absolute measurements of the second-order susceptibility $\chi^{(2)}$ of fused silica by cascading⁸ provides an additional verification of our results. The agreement with the cascading calibration values of $\chi^{(3)}(-3\omega, \omega, \omega, \omega) = (1.99 \pm 0.20) \times 10^{-22} \text{ m}^2/\text{V}^2$ at $1.064 \mu\text{m}$ and $\chi^{(3)}(-3\omega, \omega, \omega, \omega) = (1.62 \pm 0.15) \times 10^{-22} \text{ m}^2/\text{V}^2$ at $1.907 \mu\text{m}$ is excellent. In these values, an experimental error of the second-order susceptibility $\chi^{(2)}$ has also been included when compared to the original paper. The agreement between the two methods is better than we could expect from our experimental uncertainties in the THG experiments.

The error range of our absolute nonlinearity measurements overlap also with the error bars of the cascading experiments in Ref. 7 which yielded a third-order susceptibility $\chi^{(3)}(-3\omega, \omega, \omega, \omega) = (1.33 \pm 0.15) \times 10^{-22} \text{ m}^2/\text{V}^2$ at $1.907 \mu\text{m}$. However, the agreement is worse than for our own cascading experiments.

TABLE III. Third-order susceptibilities $\chi^{(3)}(-3\omega, \omega, \omega, \omega)$ of fused silica calibrated by THG measurements in various gas atmospheres.

	$\chi^{(3)}(1.064 \mu\text{m})$ ($10^{-22} \text{ m}^2/\text{V}^2$)	$\chi^{(3)}(1.064 \mu\text{m})$ (10^{-14} e.s.u.)	$\chi^{(3)}(1.907 \mu\text{m})$ ($10^{-22} \text{ m}^2/\text{V}^2$)	$\chi^{(3)}(1.907 \mu\text{m})$ (10^{-14} e.s.u.)
He	1.95 ± 0.20	1.39 ± 0.15	1.69 ± 0.25 1.52 ± 0.25	1.21 ± 0.18 1.09 ± 0.18
Ar	2.18 ± 0.20 2.16 ± 0.20	1.56 ± 0.15 1.54 ± 0.15	1.75 ± 0.25 1.57 ± 0.25	1.25 ± 0.18 1.12 ± 0.18
H ₂	1.97 ± 0.20 1.99 ± 0.20	1.41 ± 0.15 1.42 ± 0.15	1.42 ± 0.25 1.38 ± 0.25	1.02 ± 0.18 0.99 ± 0.18
N ₂	1.96 ± 0.20	1.40 ± 0.15	1.60 ± 0.25	1.14 ± 0.18
average	2.04 ± 0.20	1.46 ± 0.15	1.56 ± 0.25	1.12 ± 0.18

The comparison with the cascading experiments of Meredith and co-workers^{5,6} with $\chi^{(3)}(-3\omega, \omega, \omega, \omega) = 3.89 \times 10^{-22} \text{ m}^2/\text{V}^2$ at $1.907 \mu\text{m}$ leads to very bad agreement at first. If the second-order susceptibility $\chi_{111}^{(2)}(-2\omega, \omega, \omega) = 0.94 \text{ pm/V}$ [$d_{11}(-2\omega, \omega, \omega) = 0.47 \text{ pm/V}$], which Meredith and co-workers assumed for quartz at $1.064 \mu\text{m}$, is corrected to the currently accepted value of $\chi^{(2)}(-2\omega, \omega, \omega) = 0.60 \text{ pm/V}$ [$d_{11}(-2\omega, \omega, \omega) = 0.30 \text{ pm/V}$], the third-order susceptibility changes to $\chi^{(3)}(-3\omega, \omega, \omega, \omega) = 1.58 \times 10^{-22} \text{ m}^2/\text{V}^2$. This value is then in good agreement with the values in this paper, and with our cascading experiments.

The various calibration measurements of the third-order susceptibility at degenerate frequencies yield an averaged standard value of $\chi^{(3)}(-\omega, \omega, -\omega, \omega) = 2.04 \times 10^{-22} \text{ m}^2/\text{V}^2$ (Ref. 4) at $1.053 \mu\text{m}$. As the nonlinearity is measured at a slightly different point in the dispersion relation, $\chi^{(3)}$ does not have to coincide with our experiments, but should at least be in the same range, a requirement that is obviously fulfilled.

V. CONCLUSIONS

We have shown that it is possible to measure the absolute value of the nonlinear optical third-order susceptibility $\chi^{(3)}(-3\omega, \omega, \omega, \omega)$ by THG in a well-defined gas atmosphere with an error of 10–15%. The measurements on four different gas species are in good agreement with one another, leading to the same absolute $\chi^{(3)}(-3\omega, \omega, \omega, \omega)$ within the experimental error range. The comparison with our cascading experiments, which are completely independent of the THG measurements, discloses the same results, with deviations significantly smaller than the experimental error bars.

All these measurements enable us to define a more reliable reference value for the third-order susceptibility $\chi^{(3)}(-3\omega, \omega, \omega, \omega)$ of fused silica. Averaging the results from THG and cascading experiments, we find

$$\begin{aligned} \chi^{(3)}(-3\omega, \omega, \omega, \omega) &= (2.0 \pm 0.2) \\ &\times 10^{-22} \text{ m}^2/\text{V}^2 \quad \text{at } 1.064 \mu\text{m} \end{aligned} \quad (29)$$

and

$$\begin{aligned} \chi^{(3)}(-3\omega, \omega, \omega, \omega) &= (1.6 \pm 0.2) \\ &\times 10^{-22} \text{ m}^2/\text{V}^2 \quad \text{at } 1.907 \mu\text{m} \end{aligned} \quad (30)$$

which we propose as new standard values for fused silica. Furthermore, we can confirm the second-order susceptibility $\chi^{(2)}$ of quartz to be $\chi^{(2)}(-2\omega, \omega, \omega) = 0.60 \text{ pm/V}$ at a wavelength $1.064 \mu\text{m}$ and $\chi^{(2)}(-2\omega, \omega, \omega) = 0.56 \text{ pm/V}$ at $1.907 \mu\text{m}$.

ACKNOWLEDGMENTS

This research was supported by a grant from the ETH Research Council. We thank P. Kaatz for helpful comments in planning these experiments.

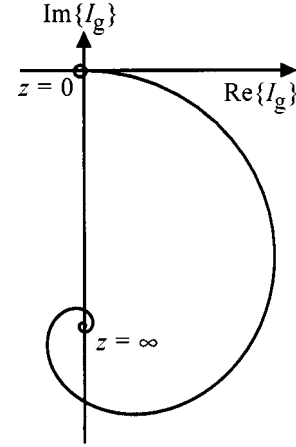


FIG. 11. Vibrational diagram for a gas medium with normal dispersion in the positive half-space $z > 0$. The generated third-harmonic field describes a spiral in the complex plane as a function of the propagation coordinate z .

APPENDIX

For the numerical integral

$$I_g(z) = \int_a^z \frac{e^{i\Delta k(z'-a)}}{(1 + iz'/z_0)^2} dz', \quad (A1)$$

various definitions are used by different authors, depending on the choice of the focus coordinates and the integration boundaries. The amplitude for all definitions stays the same, but the phase factor changes. Therefore, the measured harmonic intensity is independent of the initial notation.

Attention has to be paid at the interface of two nonlinear media. The accumulated phase of the integral in the first medium has to be correctly added to the phase in the second medium. The phase mismatch between the fundamental and harmonic wave has to persist at the interface, as neither of them experience a phase shift.

A convenient way to visualize the numerical integrals $I_g(z)$ and to increase the intuitive understanding are vibration diagrams according to Ward and New¹⁰ (see, e.g., Fig. 3). The integral $I_g(z)$ is plotted as a curve in the complex plane, with z as a running parameter. The trace starts with $z=a$ in the origin of the complex plane, and is built up by adding vector increments of the integral argument. The vector from the origin to the end point of the trace portrays the created third harmonic.

Assuming a gas medium occupying only the positive half-space $z > 0$, a numerical evaluation of the integral shows a spiral with the end point on the imaginary axis (Fig. 11). The wave-vector difference $\Delta k = 3k_\omega - k_{3\omega} = (3\omega/c)(n_\omega - n_{3\omega})$ is negative for normal dispersion $n_{3\omega} > n_\omega$ (it holds for practically all dielectrics and gases in the visible spectral region), and therefore the end point of the spiral lies on the negative imaginary axis.

The integration over the negative half-space $z < 0$ exhibits a horizontally flipped spiral. The phase $\exp(-i\Delta ka) = \exp(-i\infty)$ is not defined, which corresponds to a free rotation in the complex plane. In order to be in agreement with the spiral of the positive half-space at $z=0$, the phase is fixed by

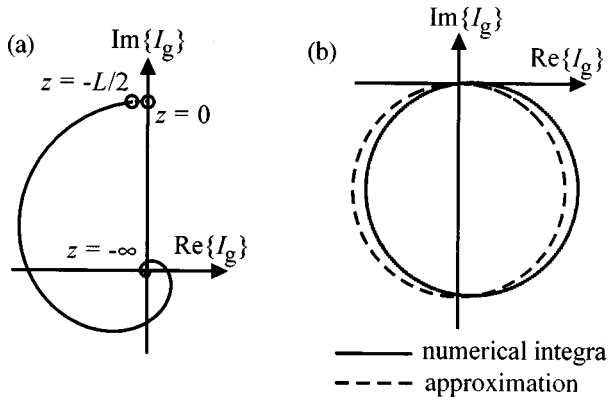


FIG. 12. Vibrational diagrams of the exact solutions and approximations used in the experimental data analysis. (a) In the gas, the numerical integral of the third-harmonic generation is conducted until $z=0$ instead of $z=-L/2$, which results in a deviation in the phase but only little in the amplitude. (b) The plane-wave approximation for the thin fused plate results in a rotation of the exact, numerically integrated solution.

$a=0$, showing a smooth curve when integrated over the whole space [Fig. 3(a)].

In the experiment the gas phase extends only until $z=-L/2$, which gives a small deviation of the phase if compared with the integration over the whole half-space $z<0$ [Fig. 12(a)]. The error in the amplitude is even smaller as one is close to the focus of the beam. For a thin fused silica plate in the beam focus, an approximation is introduced in Eq. (16), yielding a little different trace in the vibration diagram than the exact numerical integration [Fig. 12(b)].

$$I_s(L) = \int_{-L/2}^{L/2} \frac{e^{i\Delta k_s(z'+L/2)}}{(1+iz'/z_0)^2} dz' \approx \left(e^{i\Delta k_s L/2} \frac{2 \sin(\Delta k_s L/2)}{\Delta k_s} \right). \quad (\text{A2})$$

The circle of the approximation is rotated by the above-mentioned phase deviation of the gas in order to show a smooth curve at the interface. The distortion from a perfect circular shape is very minor for a thin fused silica plate.

For the positive half-space $z>0$, the same approximation as for the negative half-space applies, also resulting in a small phase difference. All three approximations are more dependent on the phase than on the amplitude of the field. As

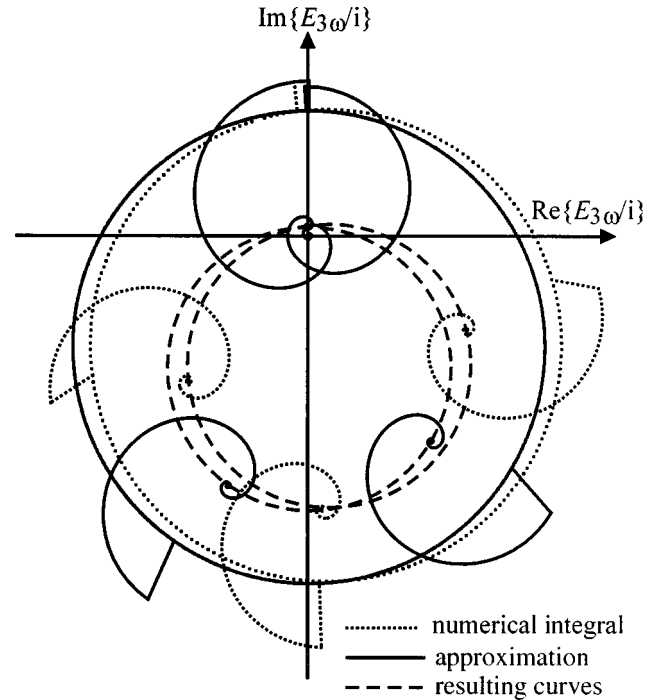


FIG. 13. Overall vibrational diagrams for the THG process in the experiment, with the third-order susceptibilities $\chi^{(3)}$ and the transmission factors included. The approximation (full line) results in a rotation of the exact vibrational diagram (dotted line). The amplitudes which are measured in a THG experiment by varying the plate thickness (dashed line) exhibit practically no differences in the two approaches.

one measures the intensity of the generated third-harmonic frequency, the phase deviations have no influence.

By also incorporating the third-order susceptibilities $\chi^{(3)}$ and the transmission factors, vibration diagrams of the total THG process can be depicted (Fig. 4).^{5,19} The diagrams for the numerical integration and the approximation are rotated with respect to one another by an angle (Fig. 13). The resulting Maker-fringe patterns created by the amplitudes show only minor differences between the exact solution and the approximation, as illustrated above. Simulations for our experimental conditions exhibit agreement better than 99% in any case. For our data analysis we consequently employed approximations [Eq. (20)] to save calculation time.

*Electronic address: gubler@iqe.phys.ethz.ch

¹F. Kajzar and J. Messier, Phys. Rev. A **32**, 2352 (1985).

²R. W. Hellwarth, Prog. Quantum Electron. **5**, 1 (1977).

³M. Sheik-Bahae, Ali A. Said, Tai-Huei Wei, David J. Hagan, and E. W. Van Skyland, IEEE J. Quantum Electron. **26**, 760 (1990).

⁴D. Milam, Appl. Opt. **37**, 546 (1998).

⁵G. R. Meredith, Phys. Rev. B **24**, 5522 (1981).

⁶B. Buchhalter and G. R. Meredith, Appl. Opt. **21**, 3221 (1982).

⁷A. Mito, K. Hagimoto, and C. Takahashi, Nonlinear Opt. **13**, 3 (1995).

⁸C. Bosshard, U. Gubler, P. Kaatz, W. Mazerant, and U. Meier, preceding paper, Phys. Rev. B. **61**, 10 688 (2000).

⁹D. P. Shelton and J. E. Rice, Chem. Rev. **94**, 3 (1994).

¹⁰J. F. Ward and G. H. C. New, Phys. Rev. **185**, 57 (1969).

¹¹G. C. Bjorklund, IEEE J. Quantum Electron. **11**, 287 (1975).

¹²H. J. Lehmeier, W. Leupacher, and A. Penzkofer, Opt. Commun. **56**, 67 (1985).

¹³D. R. Lide, *Handbook of Chemistry and Physics*, edited by David R. Lide, 73rd ed. (CRC Press, Boca Raton, FL, 1992).

¹⁴*Atomic and Molecular Physics, Magnetic Properties of Coordination and Organometallic Transition Metal Compounds*, edited by K.-H. Hellwege and A. M. Hellwege, Landolt-Börnstein, New Series, Group II, Vol. 8, (Springer-Verlag, Berlin, 1962).

¹⁵D. P. Shelton and V. Mizrahi, Phys. Rev. A **33**, 72 (1986).

¹⁶E. R. Peck and B. N. Khanna, J. Opt. Soc. Am. **56**, 1059 (1966).

¹⁷E. R. Peck and S. Huang, J. Opt. Soc. Am. **67**, 1550 (1977).

¹⁸P. J. Leonard, At. Data Nucl. Data Tables **14**, 22 (1974).

¹⁹G. R. Meredith, B. Buchhalter, and C. Hanzlik, J. Chem. Phys. **78**, 1543 (1983).